# Reversible ppt-Level Detection of Perfluorooctane Sulfonic Acid in Tap Water using Field-Effect Transistor Sensors

Yuqin Wang[1,2,3], Hyun-June Jang[1,2], Max Topel[1], Siva Dasetty[1], Yining Liu[1,2,3], Mohamed Ateia[4,5], Aaron Tam[6], Vepa Rozyyev[1,3,7], Ellie Ouyang[1], Wen Zhuang[1,2], Haihui Pu[1,2], Sang Soo Lee[2], Jeffrey W. Elam[3,7], Andrew L. Ferguson[1]*, Seth B. Darling[1,2,3]* and Junhong Chen[1,2]*

[1]*Pritzker School of Molecular Engineering, University of Chicago, Chicago, IL, USA.*

[2]*Chemical Sciences and Engineering Division, Physical Sciences and Engineering Directorate, Argonne National Laboratory, Lemont, IL, USA.*

[3]*Advanced Materials for Energy-Water Systems Energy Frontier Research Center, Argonne National Laboratory, Lemont, IL, USA.*

[4]*Center for Environmental Solutions & Emergency Response, U.S. Environmental Protection Agency, Cincinnati, OH, USA.*

[5]*Department of Chemical and Biomolecular Engineering, Rice University, Houston, TX, USA.*

[6] *Oak Ridge Institute for Science and Education (ORISE), Oak Ridge, Tennessee, USA*

[7]*Applied Materials Division, Argonne National Laboratory, Lemont, IL, USA.*

*Corresponding authors:* junhongchen@uchicago.edu, darling@anl.gov, andrewferguson@uchicago.edu

## Abstract

Widespread, persistent, and toxic per- and polyfluoroalkyl substances (PFAS) pose a major threat to both water systems and human health. Current PFAS detection methods are relatively expensive, slow, and complex. To combat PFAS contamination and meet increasingly stringent regulations of PFAS in drinking water, the development of highly sensitive and selective PFAS sensing techniques is urgently needed. Herein, we present an ultrasensitive sensing platform for perfluorooctane sulfonic acid (PFOS) detection in tap water with a reporting limit (~250 ppq) lower than the maximum contaminant level (4 ppt) set by the U.S. Environmental Protection Agency, using remote gate field-effect transistor (RGFET) sensors featuring β-cyclodextrin (β-CD)-modified reduced graphene oxide as the sensing membrane. The sensor exhibits excellent selectivity against common inorganic ions (e.g., $Na^+$, $K^+$, $Ca^{2+}$, $Cl^-$, $HPO_4^{2-}$, $SO_4^{2-}$ ) and select organic pollutants (e.g., trichloroacetic acid) in tap water. Importantly, the reversible and rapid response (< 2 min) indicates the potential of RGFET for continuous inline monitoring of PFAS. Quartz crystal microbalance results emphasize the important roles of both analyte adsorption and charge properties of analytes and buffers in generating sensing signals. The binding nature between β-CD probe and PFOS or interferent molecules, as well as the spatially resolved selectivity revealed by molecular dynamics simulations, suggest rational probe engineering strategies for future selective capture probe design**.

## Introduction

Per- and polyfluoroalkyl substances (PFAS) represent a large family of fluorinated chemicals, with

an expanding database of identified family members larger than 8,000

2

(https://comptox.epa.gov/dashboard/chemical-lists/PFASSTRUCTV3). They have been frequently used in industrial manufacturing and are present in various consumer products, owing to their unique properties including high resistance to heat and chemicals, surfactant nature, hydrophobicity, and lipophobicity[1-3]. Throughout the lifecycle of PFAS-containing products, PFAS molecules are released into the environment, transported within and across various media, and eventually enter human bodies[3, 4]. Because of the exceptionally strong carbon-fluorine bond (C-F), PFAS resist degradation under natural or biological conditions, and therefore tend to accumulate in the environment and inside human bodies[5, 6]. Extensive epidemiological studies have revealed the correlation between PFAS exposure and many adverse health effects such as compromised immune system, thyroid disease, liver damage, reproductive and developmental defects, and even cancers[6, 7].

Drinking water is a common and important pathway through which people can directly be exposed to and ingest PFAS. Multiple PFAS species have been detected in drinking water/tap water at concentrations ranging from a few ppt (ng/L) to hundreds of ppt all over the world[8, 9]. Several regulatory agencies have set guidelines and standards for certain PFAS chemicals in drinking water in response to ongoing PFAS exposure[8]. On April 10, 2024, the U.S. Environmental Protection Agency (USEPA) announced the final National Primary Drinking Water Regulation for six PFAS and established their maximum contaminant levels (MCLs) in drinking water, with an MCL of 4 ppt for perfluorooctanoic acid (PFOA) and perfluorooctane sulfonic acid (PFOS), two predominant legacy PFAS molecules (https://www.epa.gov/sdwa/and-polyfluoroalkyl-substances-pfas). The ongoing water crisis caused by PFAS pollution, and the increasingly stringent regulations emphasize the urgent need for effective monitoring of PFAS concentrations in water.

PFAS detection in tap water is challenging due to the complexity of water matrices and the relatively low concentrations of PFAS compared with co-existing ions and organic water constituents. High sensitivity and selectivity for sensors are the key requirements to achieve effective PFAS detection[10, 11]. Currently, the standard detection method based on solid-phase extraction (SPE)-enabled liquid chromatography-tandem mass spectrometry (LC-MS/MS) defined by USEPA (EPA Methods 533 and 537.1)[12, 13] can meet both requirements. However, this technique requires expensive and sophisticated instruments, well-trained personnel, and tedious procedures, which limits its prevalence in both PFAS research and real-world applications. Developing accessible and rapid PFAS sensors with satisfactory performance has become a major goal[14]. To date, most PFAS sensors presented in publications are either based on fluorescent or electrochemical sensing mechanisms[10]. Fluorescent sensors[15-17] with simple systems and large design space can render certain selectivity by designing selective probes, but their detection limit (~ppb) is typically insufficient for PFAS monitoring at environmentally relevant concentrations (~ppt). By contrast, electrochemical sensors[18-20] can measure PFAS concentrations down to sub-ppb levels; however, the PFAS sensing selectivity as a major challenge has seldom been demonstrated or achieved[10, 21]. Moreover, few of these explored sensors have shown the potential for real-time continuous sensing. Field-effect transistor (FET) sensors belonging to the electronic sensor family[22], another important category of water sensors, have been extensively studied in the detection of diverse water pollutants, including heavy metal ions[23, 24], nutrients[25, 26], and bacteria[27, 28]. The high sensitivity and readily tunable selectivity together with other advantages like fast response and portability[22] have placed FET sensors as strong candidates in water sensing compared with fluorescent or electrochemical sensors. However, to the best of our knowledge, FET sensors have never been applied to PFAS detection.

4

In this work, we demonstrate the use of a remote gate FET (RGFET) sensor to detect PFOS in tap water. With this platform, we have achieved ultra-high sensitivity for PFOS detection in tap water, excellent selectivity against inorganic ions and certain organic pollutants, and promising sensing reversibility. Quartz crystal microbalance (QCM) studies were performed to help understand the analyte adsorption at the sensing surface. To elucidate the sensing mechanism and strategize for the further improvement on the specific detection, molecular dynamics (MD) simulations were conducted to obtain a molecular level understanding of the interactions between β-CD, PFOS, and several exemplary interferent molecules. The resulting proof-of-concept, reversible FET-based PFAS sensor demonstrates the potential of using FET sensors to meet the urgent need for ultrasensitive, real-time, and continuous PFAS monitoring.

## Results

### Sensor Design & Characterization

Our RGFET sensing platform consists of three major components (Fig. 1a): a commercial metal-oxide-semiconductor field-effect transistor (MOSFET, n-type) as the transducer for sensing signals, a sensing layer on the $SiO_2$/Si substrate called a remote gate (RG, remotely connected with the gate electrode of the MOSFET) where the sensing events occur, and an Ag/AgCl reference electrode for stabilizing the global gate potential (*cf.* Supplementary Fig. 1 for the real experimental set-up). Compared with conventional back gate FET sensors, RGFET sensors have fewer side reactions by avoiding direct contact of sample solutions with the transducing channels[29, 31]. Two-dimensional (2D) reduced graphene oxide (rGO) with high specific surface area and desirable probe anchoring sites was used as the sensing membrane. β-cyclodextrin (β-CD), a proven effective probe for PFAS capture via host-guest interactions[32-34], was chosen to modify the

rGO surface with the help of a 1-pyrenebutyric acid *N*-hydroxysuccinimide ester (PBASE) linker to enhance the sensor specificity to PFOS. The structures of PFOS and mono-$NH_2$-β-CD-PBASE (β-CD probe + PBASE linker) as well as the equivalent circuit of this platform are shown in Fig. 1a. We quantify the shifts in FET transfer curve as our sensing signals (Fig. 1b), which can be changed by the surface potential $\phi_s$ at the solution/sensing membrane interface during the sensing process.



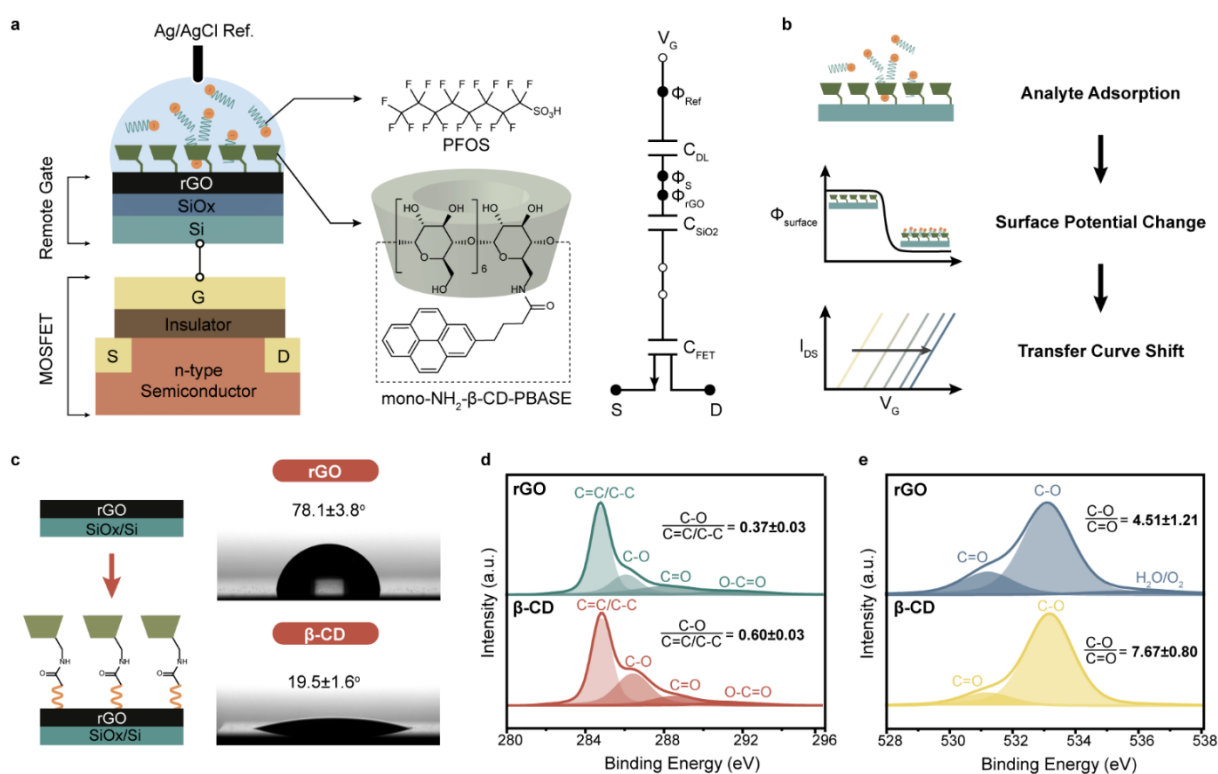**Fig. 1|Sensor design & characterization of remote gate (RG) electrodes. a**, Illustration of RGFET sensor structure (left), chemical structures of PFOS, β-CD probe linked with PBASE linker (middle), and equivalent circuit of RGFET[29, 30] (right) where the only factor that is supposed to change during the sensing process is $\phi_s$ (surface potential at the solution/sensing membrane interface). **b**, Sensing mechanism of RGFET sensors. Sensing starts with analyte adsorption onto surface probes on the sensing membrane. The accumulation of analytes induces a potential change

at the interface ($\Delta\phi_s$), which is transduced and detected by the metal-oxide-semiconductor FET (MOSFET) and leads to shifts in the FET transfer curves characterized by the FET threshold voltage ($V_{th}$). **c**, Comparison of the water contact angles (WCA) of rGO RG electrodes before and after functionalization with mono-$NH_2$-β-CD probe (the top labels represent the chemistry of the outmost layer of the electrodes). **d**, XPS C1s peak of rGO and β-CD RG electrodes. **e**, XPS O1s peak of rGO and β-CD RG electrodes. The data in **c, d,** and **e** are presented as mean values ± the standard error of the mean (S.E.M.) for n = 3.

The fabrication of RG electrodes followed a step-by-step process (Supplementary Fig. 2 and Methods). The successful preparation of the desired RG electrodes was confirmed by water contact angle (WCA) measurement, Raman spectroscopy, and X-ray photoelectron spectroscopy (XPS) (Supplementary Fig. 3 and Fig. 1c-e). The effective surface modification with β-CD probes was validated by the significant decrease in the WCA (Fig. 1c) from rGO RG surface (78.1±3.8°) to β-CD RG surface (19.5±1.6°) owing to the abundant hydroxyl groups in β-CD probes, and the discernible increase (from rGO RG to β-CD RG) in the ratio of C-O bond, which is a major feature of the β-CD molecule, to C=C/C–C bond (from 0.37±0.03 to 0.60±0.03) and C=O bond (from 4.51±1.21 to 7.67±0.80) from the XPS C 1s peak (Fig. 1d) and O 1s peak (Fig. 1e). Higher hydrophilicity is also beneficial to create a stable water/solid interface, which can increase signal stability and reduce the sensor stabilization time during the measurement. A continuous film formed by modified rGO flakes and some aggregates can be seen in the scanning electron microscopy (SEM) image for β-CD RG surface (Supplementary Fig. 4a). The resulting sensing layer had a thickness of ~9.3 nm and a surface roughness of ~3.0 nm according to atomic force microscopy (AFM) analyses (Supplementary Fig. 4b,c).

**Characteristics of RGFET sensors & PFOS responses in tap water**

After assembling the prepared β-CD RG electrode with MOSFET to construct the RGFET sensing system, a careful stabilization process was performed before testing any water samples to minimize the influence of background drift (Supplementary Fig. 5). The threshold voltage ($V_{th}$) of RGFET sensors is sensitive to surface materials due to their work function differences (Fig. 2a and Supplementary Fig. 6) resulting either from different material types (e.g., $SiO_x$ vs. GO) or charge transfer after surface conjugation (e.g., pristine rGO vs. β-CD-modified rGO). Surface materials also have an impact on the transconductance ($G_m$) of the RGFET (Supplementary Fig. 6) since their surface charges affect the stabilization process. The β-CD-coated RGFET could maintain a similar $G_m$ (~88 μS) to that of the pristine MOSFET, suggesting that these surface functionalization processes didn't impact the intrinsic sensitivity of the MOSFET device. Prior to the PFOS detection, our RGFET sensors were first benchmarked against pH interference (Supplementary Fig. 7). This pH or proton sensitivity (~36 mV/pH) comes from both rGO membranes and mono-$NH_2$-β-CD-PBASE groups and cannot be eliminated for this material system. Therefore, a pH buffer is necessary for sample preparation to ensure a stable pH value during the sensing process. We observed that our tap water acts as a natural buffer, maintaining a stable pH that does not change with different concentrations of spiked analytes considered here or during ~one week sample storage (Supplementary Table 1), and thus the tap water was used to prepare test sample solutions. The potential applications of six other buffers were also explored, but they were not as effective as the fresh tap water in terms of generating measurable sensing signals likely due to the resulting relatively high baseline $V_{th}$ of the RGFET (Supplementary Discussions 1,2, Supplementary Figs. 8,9, and Supplementary Tables 1,2).
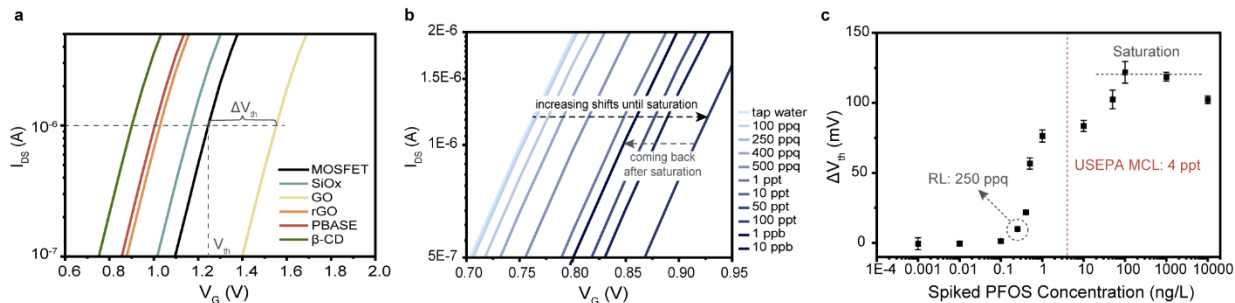
**Fig. 2|Characteristics of RGFET sensors & PFOS responses in tap water. a**, Representative transfer curves (20$^{th}$ cycle) corresponding to various RG surfaces exposed to the same sample (pH=7 buffer) with $V_{th}$ defined at a drain-source current of $1 \times 10^{-6}$ A and used to quantify the transfer curve shifts (as $\Delta V_{th}$) caused by $\Delta \phi_s$. **b**, Representative transfer curves (20$^{th}$ cycle) of PFOS solutions with different concentrations in tap water on β-CD-functionalized RG surface. **c**, Sensor response curve of PFOS in tap water (the reporting limit (RL) is 250 ppq). It should be noted that the concentrations in **b** and **c** refer to the additional PFOS concentrations spiked into the blank tap water. The real PFOS concentration is the sum of the background PFOS in the blank tap water and the additionally spiked PFOS. The sensor response $\Delta V_{th}$ reported here is derived from the differential response between spiked and blank tap water samples. The data in **c** are presented as mean values ± S.E.M. for n = 3-6.

The accuracy of PFOS concentrations is critical to obtaining a reliable calibration curve. To this end, the standard EPA methods (see Methods section) for drinking water (LC-MS/MS) was used to check the real concentrations of prepared PFOS samples and the results show that the measured concentrations of most samples are close to the targeted concentrations (Supplementary Table 3). Although there are low background PFOS concentrations in the blank tap water (~ 2 ppt measured by LC-MS/MS), their interactions with the sensing surface have already been

9

equilibrated after the sensor stabilization process, and adding blank tap water does not produce any further sensing signal (Supplementary Fig. 10). Thus, we attribute the observed sensor responses to the adsorption of additionally spiked PFOS.

Fig. 2b shows the representative transfer curves for PFOS at different concentrations, where we can see the transfer curves shift to the higher $V_G$ direction when relative PFOS concentrations increase from zero (blank tap water) to a saturation point around 100 ppt, and then shift back after saturation (from 100 ppt to 10 ppb). The decreasing signals after saturation are typical of FET device, which could be attributed to the synergistic effects of the increased ion concentrations, multilayer analyte adsorption, and the decreased $\Delta\sigma$ (surface charge density change)-dependence of the $\Delta\phi_s$ in certain regions of the $\sigma$-$\phi_s$ curve after the saturation point according to the Grahame equation[35] (Supplementary Discussion 2).

The sensor's response curve for PFOS in tap water is presented in Fig. 2c. The detection range of this device is from a few hundred of ppq to around 100 ppt, which matches well with the realistic concentration range of PFOS in natural waters[8]. The reporting limit (RL, defined as the reported lowest PFOS concentration that can be detected in this work) of this device is around 250 ppq and reaches a level lower than the USEPA's MCL for PFOS (4 ppt), suggesting the superior sensitivity of the sensors.

**Selectivity and reversibility**

To better evaluate the application potential of our sensing platform, the selectivity of our RGFET sensing devices against structural analogues (OA, OSA, PFO, and PFOA), representatives of organic dyes (MB), disinfection byproducts (TCAA), and common inorganic ions ($Na_2SO_4$,

K$_2$HPO$_4$, CaCl$_2$) in tap water was measured at the same molar concentrations (0.2 nM) for all analytes (Fig. 3a). The results show that our sensors possess outstanding selectivity (i.e., no response) against inorganic ions, moderate selectivity (~20-30% of the PFOS signal) against MB, TCAA, and PFOA, and relatively poor selectivity (~50% of the PFOS signal) against some structural analogues like OSA. Sensor testing at higher interferent concentrations (0.2 nM – 2000 nM for organic interferents; 100 ppb – 10 ppm for inorganic ions) and environmentally relevant PFOS concentrations (1–100 ppt) were also performed as a stress test (Supplementary Fig. 11). The signal for PFOS at 10 ppt (20 pM) was compared to the responses for organics at 20 nM and inorganic ions at 1 ppm (environmentally relevant concentrations of these ions[36]), and the results indicated our sensors can maintain moderate selectivity against all these interferents even when their concentrations are more than 10$^3$ times higher than the PFOS concentration (Supplementary Fig. 12). Sensor response of a common co-existing surfactant, sodium dodecyl sulfate (SDS), was recorded as well in the range of 100 ppt to 1 ppm. Our devices showed strong responses to SDS, and there was almost no selectivity between PFOS and SDS (Supplementary Fig. 13), which indicates that we need to either modify the β-CD probe to introduce more favorable interactions towards PFAS such as fluorophilic interaction[32, 37, 38] or find better surface capture probes to enhance the sensor selectivity against especially challenging interferents like SDS.
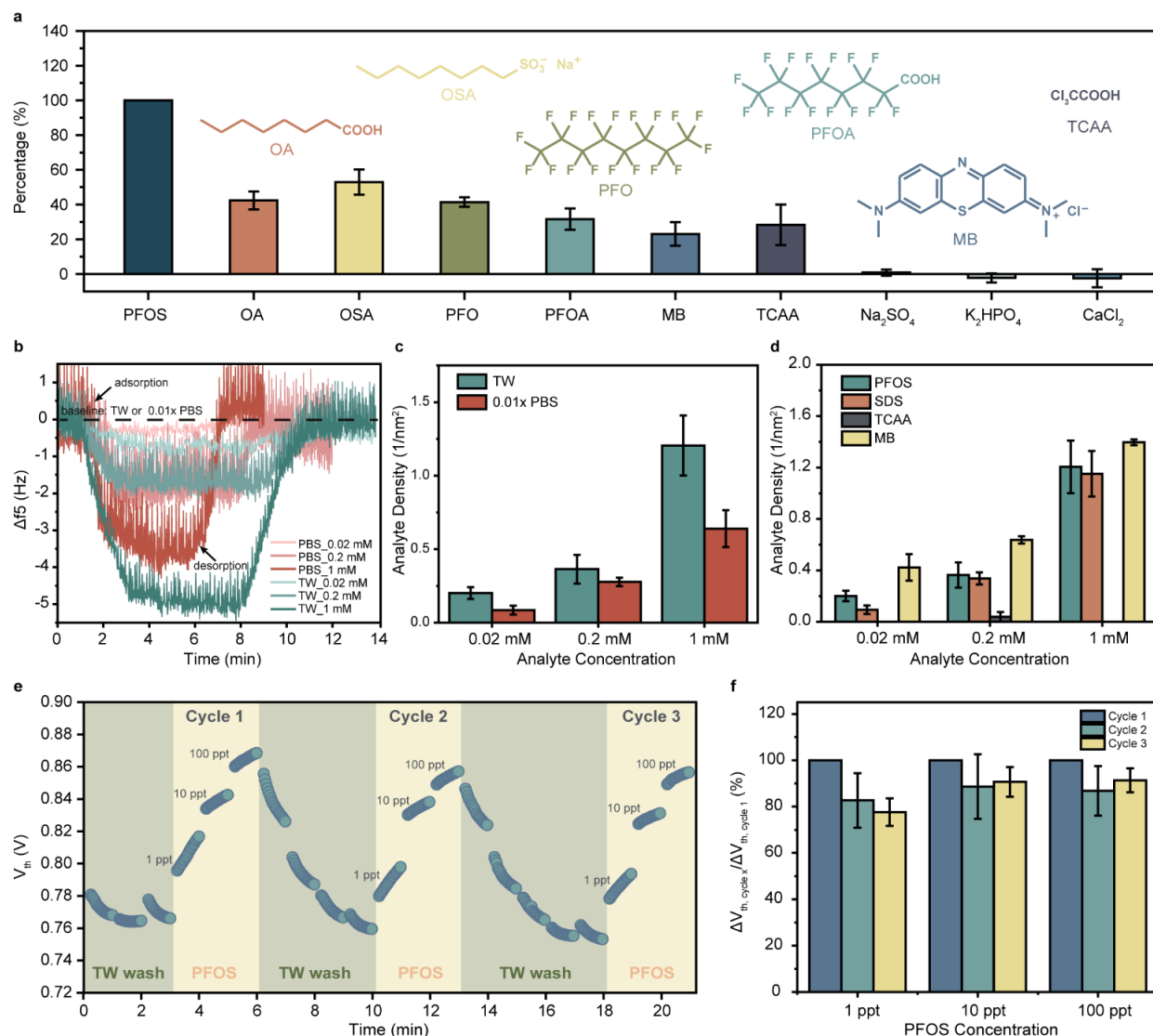
11

**Fig. 3|Selectivity & reversibility of RGFET sensors. a,** Sensor responses to PFOS, six organic interferents (with chemical structures), and three inorganic ions all at 0.2 nM in terms of the percentage response compared to the PFOS response (100%) in tap water on β-CD RG surface. Octanoic acid (OA), 1-octanesulfonic acid sodium salt (OSA), perfluorooctane (PFO), and perfluorooctanoic acid (PFOA) were chosen as the structural analogues to PFOS. Methylene blue (MB) and trichloroacetic acid (TCAA) were selected as representatives of organic dyes that can bind with β-CD[39] and disinfection byproducts, respectively. Sodium sulfate ($Na_2SO_4$), potassium phosphate dibasic ($K_2HPO_4$), and calcium chloride ($CaCl_2$) were used to represent common

12

inorganic ions in tap water. **b**, QCM curves of PFOS adsorption and desorption process (washing with blank buffer) in tap water (TW) and in 0.01× PBS buffer. During the desorption process, the blank buffer (TW or PBS) was flowed across the surface. **c**, Comparison of the adsorbed PFOS densities in TW and 0.01× PBS. **d**, Comparison of the surface adsorbed densities for 4 analytes (PFOS, SDS, TCAA, MB) in TW. **e**, A typical sensor response curve for the reversibility testing process (3 cycles). **f**, Sensor responses to PFOS in tap water on β-CD RG surface for 3 testing cycles in terms of the percentage response compared to the 1st cycle. The data in **a**, **c**, **d** and **f** are presented as mean values ± S.E.M. for n = 3-6.

Sensing signals of FET devices not only depend on analyte adsorption but are also influenced by the charge properties of different analytes, sensing materials, and buffers. QCM with dissipation monitoring (QCM-D), which monitors in real time the mass changes on the surface through detecting resonance frequency change, can help us understand the adsorption-related analyte/surface interactions in buffers[40, 41].To simulate the sensing surface, similar rGO films were deposited on QCM sensors (Supplementary Fig. 14), which have comparable surface hydrophobicity (~78.3°), surface roughness (~3.8 nm), and layer thickness (~7.4 nm) to that of the RGFET sensor surface. We monitored the surface functionalization processes of PBASE linker and $NH_2$-β-CD probe and calculated their surface probe densities to be 1.7 molecules/$nm^2$ and 1.8 molecules/$nm^2$, respectively (Supplementary Figs. 15,16).

PFOS samples prepared in both PBS buffer and fresh tap water were flowed across the simulated sensor surface to investigate if PFOS adsorption is a determining factor for the different sensing signals of RGFET in PBS buffer (no signal) and in tap water (strong signals). At selected concentrations (0.02 mM, 0.2 mM, 1 mM), PFOS adsorption occurs in both buffers, which suggests that adsorption is not the cause for undetectable sensing signals in PBS. However, the

13

adsorbed PFOS density in tap water is higher than that in the PBS buffer (Fig. 3b,c and Supplementary Fig. 17). We suspect that the enhanced PFOS adsorption in tap water could be related to the pre-deposited species from tap water on the QCM sensor surface during the QCM baseline stabilization process (Supplementary Fig. 18), because tap water has many divalent cations and hydrocarbons that can potentially enhance the electrostatic and hydrophobic interactions with PFOS[42], respectively.

The adsorption densities of four analytes in tap water, including PFOS, SDS, TCAA, and MB, were also compared to elucidate the mechanism behind the selectivity of our RGFET sensors (Supplementary Fig. 19 and Fig. 3d). PFOS and SDS have similar adsorption densities (except at 0.02 mM where the adsorption of PFOS is greater), indicating that SDS and PFOS may have similar binding affinities toward the sensing surface. In contrast, adsorption of TCAA was not observed by QCM, which may explain the weaker sensing signal of TCAA in our RGFET sensors as adsorption is the first step. However, MB exhibits even higher adsorption density than PFOS and SDS (especially at lower concentrations) despite its much weaker sensing response. This suggests that the sensing signals for MB in RGFET sensors are governed by not only the adsorption of MB but also its charge property. Overall, the findings from the QCM studies emphasize the important roles of analyte adsorption, analyte charge properties, and buffer properties in registering enough sensing signal.

The observed reversible adsorption/desorption process of PFOS through QCM at the simulated sensor surface in tap water (Fig. 3b) also suggests the reversible sensing potential of our RGFET sensors. This is further demonstrated using our RGFET devices with real-time responses to fluctuating PFOS concentrations, which indicates that PFOS sensing signals can be readily reversed by simply washing the surface with blank tap water (Fig. 3e). After three cycles, the

14

sensors can maintain ~80-90% of the original PFOS responses in the 1st cycle (Fig. 3f), suggesting the potential of our RGFET sensors for on-site and continuous PFOS monitoring applications.

**MD simulations of the interaction between analytes and the β-CD probe**

All-atom classical MD simulations were employed to gain molecular-level insight into the structure and thermodynamics of the bound complex between the PFOS analyte or the interferents SDS and TCAA with β-CD probes, identify preferred bound configurations, and resolve the molecular basis for probe sensitivity and selectivity for PFOS (Fig. 4). The free energy landscape for binding of the PFOS, SDS, and TCAA with a β-CD probe was mapped out through the potential of mean force (PMF) (r, z) describing the relative free energy of different (r, z) configurations of the probe-target system in the radial separation r and axial separation z of the molecular centers of mass within a coordinate frame centered on the cyclodextrin probe (Fig. 4d and Supplementary Fig. 20). It can be seen from Fig. 4a-c that β-CD's ~0.65 nm diameter cavity is sufficiently large to accommodate any of PFOS, SDS, or TCAA within the cavity, and in all cases the thermodynamically preferred state is for the target guest to reside within the cavity of the probe host. For quantitative comparison, we then calculated the values of the standard state (i.e., at a concentration of $C^{\Theta} = 1$ M) binding free energy $\Delta G^{\Theta}$ and binding constant $K_b$ for each of the three systems (Table 1, Supplementary Fig. 21, and Supplementary Tables 4,5). $K_b^{PFOS}$ (~$10^6$, which is in approximate agreement with the experimental value[43] of ~$10^5$) is approximately one order of magnitude larger than $K_b^{SDS}$ and almost five orders of magnitude larger than $K_b^{TCAA}$. The results are generally consistent with the trend of surface adsorption densities observed in QCM studies where the adsorption of PFOS and SDS are much greater than that of TCAA on β-CD functionalized

15

sensing surface. Although the calculated binding constant for PFOS is one order of magnitude greater than that of SDS, the observed similar adsorption from QCM and similar sensor signals from RGFET sensors for PFOS and SDS could be attributed to their non-specific adsorption onto the rGO membrane, averaging the adsorption behavior.
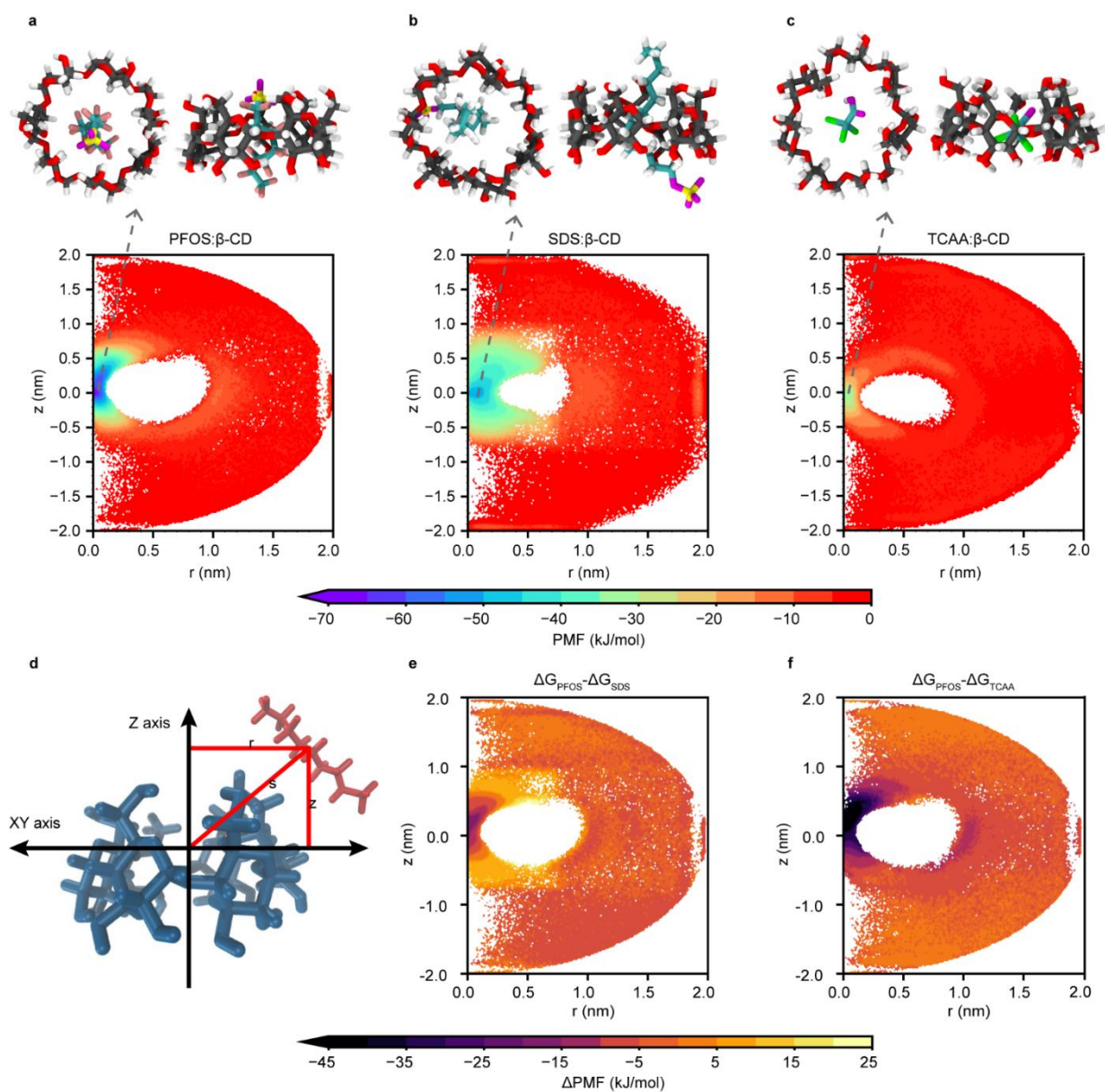


**Fig. 4|MD simulations of PFOS, SDS and TCAA molecules binding with a β-CD probe.** Potential of mean force (PMF) landscapes PMF (r, z) are constructed in the radial separation r and

16

axial separation z of the molecular centers of mass. PMFs (**a-c**, bottom) with the molecular snapshots (**a-c**, top left: top view, top right: side view) of thermodynamically preferred bound configurations for **a**, β-CD–PFOS. **b**, β-CD–SDS. **c**, β-CD–TCAA. **d**, Illustration of the cyclodextrin-centric coordinate frame. Spatially resolved selectivity map represented by the difference between the PFOS target and the two interferents in PMF profiles corresponding to the interaction with β-CD (**e-f**). **e**, $\Delta PMF^{(PFOS-SDS)}$ (r, z) = $PMF^{PFOS}$ (r, z) - $PMF^{SDS}$ (r, z). **f**, $\Delta PMF^{(PFOS-TCAA)}$ (r, z) = $PMF^{PFOS}$ (r, z) - $PMF^{TCAA}$ (r, z). Large negative values of $\Delta PMF^{PFOS-interferent}$ (r,z) indicate regions of strong selectivity for PFOS, whereas large positive values correspond to regions of strong selectivity for the interferent. For visualization convenience, the arbitrary additive constant for each PMF in **a-c**, reflecting our ignorance of the absolute free energy scale, is specified such that the free energy of the far-field, non-interacting region (s > 1.2; $s = \sqrt{r^2 + z^2}$ ) is set to zero. The location (r = 0 nm, z = 0 nm) corresponds to a configuration in which the target molecule resides within the pore of the probe and the centers of mass of the target and that of the oxygen and carbon atoms in the narrow-side plane of each of the 6-sided D-glucose units of the β-CD probe are coincident. The white region in each plot corresponds to the prohibited region due to excluded volume overlaps of the target molecule and the cylindrical wall of the probe. The white region around the edge of each plot corresponds to the far-field region that was unsampled under our funnel meta dynamics approach that focused computational sampling on the near-field region. In all cases the narrow end of the β-CD probe is oriented towards positive z values and the broader end towards negative z values. Molecular snapshots corresponding to the thermodynamically preferred bound configuration are presented for each system viewed from the side and above (narrow side facing up). All renderings were constructed using VMD 1.9.4[44].

**Table 1**. Calculated binding constants $K_b$ for the PFOS analyte and both SDS and TCAA interferents with the $\boldsymbol{\beta}$-CD probe using enhanced sampling all-atom classical MD simulations. The selectivity of PFOS relative to both SDS and TCAA is quantified by the ratio of the binding constants $K_b^{PFOS}/K_b^{interferent}$.

| $\beta$-cyclodextrin | $K_b$ | $K_b^{PFOS}/K_b^{interferent}$ |
|:---:|:---:|:---:|
| PFOS | $(2.15 \pm 0.05) \times 10^6$ | N/A |
| SDS | $(6.46 \pm 0.04) \times 10^4$ | $(3.32 \pm 0.05) \times 10^1$ |
| TCAA | $(7.04 \pm 0.05) \times 10^0$ | $(3.05 \pm 0.04) \times 10^5$ |

Spatially resolved selectivity (Fig. 4e,f) permits a greater understanding of differences in binding mechanisms and affinities. The fluorinated backbone of the PFOS molecule appears to elicit strong van der Waals interactions with the cavity walls. In comparison, the hydrogens along the backbone of SDS appear not to interact with the entirety of the cavity of the β-CD probe as efficiently as PFOS. These differences in van der Waals radii of fluorine versus hydrogen result in a relatively rigid PFOS molecule in the β-CD cavity, only able to access a limited number of strongly bound configurations and a looser fit of SDS in the cavity, and promote strong selectivity for PFOS near the center of the cavity ($s = \sqrt{r^2 + z^2}$ < 0.4 nm) where the mean $\Delta PMF^{PFOS-SDS}$ (r, z) $\approx$ -7.26±0.05 kJ/mol (Fig. 4e). Further away from the origin in the region 0.4 nm < s < 1.1 nm, binding of SDS is preferable to PFOS with a mean $\Delta PMF^{PFOS-SDS}$ (r, z) $\approx$ 6.36±0.05 kJ/mol. In the far field regime for s > 1.1 nm, $\Delta PMF^{PFOS-SDS}$ (r, z) approaches 0 kJ/mol as expected. We propose that this spatially resolved selectivity may be valuable in guiding rational engineering of the probe to promote stronger PFOS-β-CD interactions relative to SDS-β-CD interactions over the full range of binding positions.

18

In contrast, $\Delta\text{PMF}^{\text{PFOS-TCAA}}$ (r, z) is negative over the entire s < 1.2 nm region of bound configurations, indicating a global preference for PFOS relative to TCAA over all binding sites on the probe (Fig. 4f). This can likely be understood as the longer PFOS backbone providing stronger van der Waals interactions with the interior probe wall than the relatively smaller TCAA. The larger van der Waals radius of the chlorines on the backbone of TCAA relative to the hydrogens on the SDS backbone limit the ease of TCAA passing through the β-CD cavity. Consequently, TCAA does not benefit from the large number of possible bound configurations with the β-CD probe that SDS does. This effect, combined with the shortness of the TCAA chain, two carbons compared with eight for PFOS, produces an overall weaker binding affinity of TCAA with β-CD compared with PFOS.

Finally, inspection of the PFOS/β-CD bound complex indicated that the fluorinated backbone tends to occupy the cavity leaving the charged head exposed into solvent. This suggests that there may be an opportunity to further enhance the PFOS binding constant by engineering the lip (especially at the broader opening side of the probe as suggested by the thermodynamically preferred binding conformation) of the β-CD probe to promote favorable interactions (potentially electrostatic interactions) with the PFOS head and/or modifying the interior wall of β-CD cavity to strengthen the interactions with the PFOS backbone (potentially through fluorophilic interactions).

## Conclusions

We have demonstrated the reversible and fast detection (< 2 min) of PFOS in untreated tap water using an RGFET sensor with β-CD-modified rGO as the sensing surface. The RGFET sensor

19

exhibits a reporting limit of ~250 ppq, which is much lower than the MCL of 4 ppt for PFOS set by the USEPA, and a detection range from 100s ppq to 100s ppt that matches well with environmentally relevant PFOS concentrations. The reversible adsorption of PFOS at the sensing surface in tap water was validated by QCM. Our sensors showed excellent selectivity against common inorganic ions in tap water and good-to-moderate selectivity against several organic interferents like TCAA. However, the limited selectivity against certain structural analogues like SDS suggests the need of molecular probe engineering to enhance the selectivity by hindering the adsorption of such interferents. The spatially resolved selectivity from all-atom MD calculations suggests a global binding preference of β-CD for PFOS over TCAA, and further suggests that a higher selectivity toward PFOS against SDS can be achieved if the binding sites for both analytes can be restricted to the area close to the center of the β-CD cavity. Future work should focus on enhancing the selectivity by rational engineering of the rim/interior wall of the β-CD, applying other selective probes, and/or making sensor arrays, thereby realizing the full potential of this FET sensing platform for ultrasensitive, selective, on-site and continuous monitoring of PFOS in water.

## Methods

### Fabrication and characterization of RG electrodes

The fabrication of RG electrodes was modified from previous work[29]. Firstly, a silicon wafer (University Wafer, P-type B doped 4" Si Wafers w/ 300 nm Wet Thermal Oxide) was sonicated in acetone (Sigma-Aldrich) and isopropanol (Sigma-Aldrich) for 5 min sequentially. After being dried under $N_2$, the wafer was treated with oxygen plasma for 120 s, and then sonicated in deionized (DI) water for 5 min. The cleaned wafer was immediately immersed in a 5 vol% APTES

(Sigma-Aldrich) ethanolic solution for ~ 2 h. The resulting wafer was rinsed with ethanol and dried with $N_2$. A monolayer GO dispersion (ACS Material, 10 mg/mL in water) was diluted with DI to form a 0.24 mg/mL solution, which was sonicated for ~ 30 min before use. After preheating the cleaned wafer on a hot plate at 120 °C for ~20 min, ~16.4 mL of the diluted GO dispersion was poured onto the wafer surface to cover the whole area of the wafer while keeping heating the wafer at 120 °C. After all the water in the GO dispersion evaporated, the resulting GO coatings showed two distinct areas with blue and black colors, corresponding to few-layer GO and GO film, respectively (Supplementary Figure 3a). Only the thinner area (few-layer GO) was used for further modification. The coated wafer was cut into small pieces (each having $\geqslant 1$ cm$^2$ surface area to hold sample droplets) and annealed in a tube furnace (Thermo Scientific Lindberg/Blue M Mini-Mite) at 400 °C under $N_2$ for 1 h. Afterward, the rGO-coated chips were immersed in 10 mg/mL PBASE (Santa Cruz Biotechnology) solution in dimethylformamide (DMF, Sigma-Aldrich) for 2 h and then rinsed with DMF and dried with $N_2$. Finally, 10 mM $NH_2$-β-CD (BOC Sciences) water solution was added onto the PBASE-modified chips and reacted overnight (~15-18 h). Rinsing the chips with DI and drying them using $N_2$ gave the final β-CD RG electrodes.

Water contact angle (WCA) measurements were conducted using a tensimeter (Biolin Scientific Theta Flex) to determine the surface hydrophobicity of the prepared RG electrodes. Raman microscopy (Renishaw inVia) was used to confirm the deposition of GO/rGO. XPS measurements were conducted to analyze the surface chemical compositions (Thermo Fisher k-Alpha+, using the Thermo Fisher Avantage software (v.5.977, Build 06436) for data processing and analysis). The obtained XPS spectra were referenced to the C 1s peak at 284.8 eV. The X-ray source was microfocused monochromatic Al Kα (1,487 eV) with a spot size of 400 μm. A pass energy of 200.0 eV and a step size of 1.000 eV were used for the survey scan, and a pass energy

of 50.0 eV and a step size of 0.100 eV were used for a high-resolution scan. The deconvolution of high-resolution XPS spectra was performed by the Powell peak fitting algorithm with mixed Gaussian–Lorentzian line shapes and a Smart background. Surface morphology was characterized by SEM at 3 kV (FEI Nova 600 NanoLab focused ion beam SEM). The surface roughness and thickness of rGO RG and β-CD RG were measured using AFM (Cypher-ES and MFP-3D models, Asylum Research, Oxford Instruments) in tapping mode. AC240TSA-R3 (Oxford Instruments) tips with a typical resonant frequency of 70 (50−90) kHz, tip radius of 7 nm, and spring constant of 2 (0.6–3.5) N/m were used for Cypher-ES and PPP-NCHR (Nanosensors[TM]) tips with a typical resonant frequency of 330 (204–497) kHz, tip radius of <10 nm, and spring constant of 42 (10 – 130) N/m were used for MFP-3D.


**Preparation and analysis of analyte samples**

To prepare PFOS (Santa Cruz Biotechnology) samples for sensor testing, 10 mg PFOS was dissolved in 100 mL blank buffers in HDPE bottles (Thermo Scientific) to form a stock solution of 100 ppm and sonicated at 40 °C for 30 min. This stock solution was then diluted step-by-step to produce PFOS solutions with targeted concentrations from 1 ppq to 10 ppb in 15 mL PP tubes (VWR). For QCM samples, a stock solution of 1,000 ppm was made by adding 10 mg PFOS in 10 mL blank buffers in 15 mL PP tubes (VWR), which was further diluted to form solutions from 0.02 mM to 1 mM in 15 mL PP tubes (VWR). We note that the concentrations used in the QCM study are higher than those in the sensor testing due to the lower detection limit of the QCM instrument; yet, QCM tests provide relevant mechanistic insights by comparing the adsorption behavior at the same concentrations under various situations. After preparing samples at each concentration and before further dilution, the resulting solution was sonicated at 40 °C for 30 min.

For the buffers, fresh tap water was collected at our labs located at Argonne National Laboratory. PBS, MES, and Bis-Tris buffers (0.1x or 0.01x) were prepared by diluting the stock solution or solids (all from Sigma-Aldrich) in DI water. The pH of each prepared sample was tested using a pH meter (OHAUS™ Aquasearcher™ pH Meter AB41PH) to make sure the pH is the same for all the samples prepared in the same buffer. All the samples were freshly prepared before sensor testing and would not be stored over 1 week except the one that was deliberately kept > 1 week to investigate the influence of tap water storage. Other analyte solutions including SDS, OA, OSA, PFO, PFOA, MB, TCAA, $Na_2SO_4$, $K_2HPO_4$, and $CaCl_2$ (all from Sigma-Aldrich) were prepared and stored in the same way as for PFOS samples.

PFOS concentrations were measured using LC-MS/MS. low concentration samples between 1-100 ppt, solid phase (SPE) extraction was used. Before SPE, the internal standard, MPFAC-24ES, was aliquoted to the sample containers as received to obtain an expected concentration of 40 ng/L. SPE was performed on the experimental samples corresponding QC samples (Laboratory Blank, Laboratory Fortified Blank, and Laboratory Fortified Sample Matrix). 4 mL of 1% methanolic ammonium was passed through the WAX cartridges for final extraction and captured into respective 15 mL falcon tubes. Each sample was diluted to 4 mL final volumes using 0.3% methanolic ammonium hydroxide. 10 μL of acetic acid was aliquoted to each sample for pH adjustment. It was assumed that all PFOS and internal standard reached the 4 mL final volume extraction.

For high concentration samples more than 100 ppt, aliquots were diluted to a final volume of 10 mL (1000x dilution) with the 1:1 reagent water: methanol solution. Due to the high concentration of the 100 ppm and 500 ppm samples, secondary dilutions were performed. The internal standard, MPFAC-24ES, was aliquoted to each experimental sample for an expected

23

concentration of 200 ppt. After addition of internal standard, the experimental samples were filtered using pre-cleaned 0.2-micron filters. Finally, 10 µL of acetic acid was added to each sample for pH adjustment.

Calibration standards and QC samples for LC/MS/MS analysis were prepared with the native standard solutions (PFAC30-PAR) and mass-labeled isotopic standard solutions (internal standards; MPFAC-24ES, M3HFPO-DA) from Wellington Laboratories, Guelph, Ontario, Canada. PFAC30-PAR contains 36 PFAS compounds at 1.0 µg/mL each. MPFAC-24ES contains 19 mass-labeled PFAS compounds at 1.0 µg mL-1 each, and M3HFPO-DA contains one mass-labeled PFAS compound at 50 µg/mL. Calibration concentrations ranged from 5 to 10,000 ng/L (ppt) for each analyte present in the native standard solutions. Aliquots (200 µL) from the calibration standards, QC samples (calibration blanks and calibration controls), and all experimental samples (4 mL extracts) were transferred to LC vials directly prior to the injection sequence. All samples were vortexed before aliquoted to vials. Samples were analyzed on a Waters LC/MS Micro run time with a starting and ending eluent composition of 98% Eluent B (2 mM ammonium acetate in 95:5 water: acetonitrile) and 2% Eluent A (HPLC grade acetonitrile). Calibration was calculated for all analytes with compound analysis being accepted for calibration curves of $R^2$ (>0.99) for each analyte. The Minimum Reporting Limit (MRL) for the analyte was established by the lowest concentration calibration standard that agrees within 50% of the true concentration. All collected data resulted in concentrations above the MRL, satisfying the QC requirement. Final Concentrations of QC samples and experimental samples have passed QC requirements. Results are reported as Total PFOS (TPFOS).

The selected cation concentrations in the tap water were analyzed using an inductively coupled plasma optical emission spectroscopy (Thermo Scientific, iCAP PRO X ICP-OES Duo).

24

The carbon contents in the tap water were measured using a total organic carbon analyzer (Shimadzu, TOC-L). These measurements were done following the standard operating procedure of each instrument.

**Sensor testing**

A commercial Si-based n-type MOSFET (CD4007UB) was connected to the fabricated RG electrodes and used as a transducer. During the measurement, one drop (~30 µL) of sample solution was placed on the RG surface and connected with an Ag/AgCl reference electrode (Gamry Instruments) to apply the gate bias for all measurements (Supplementary Fig. 1c). All transfer curves were measured using either a Keithley 4200A or a Keysight B1500A semiconductor analyzer with a drain voltage set at 50 mV and gate voltages scanning from 0 to 1.5 V. Transfer curves of the RGFET were repeatedly measured for 20 cycles for each sample droplet. The $V_{th}$ was calculated as the gate voltage corresponding to drain current of 1 µA in each transfer curve. The $V_{th}$ of the 20$^{th}$ cycle was used for data comparison. The $G_m$ of each RGFET was calculated at its maximum value.

Sensor stabilization using the baseline solution (the blank buffer) was performed before any sample measurement (Supplementary Fig. 5). For the samples with the same analyte but different concentrations (Fig. 2b,c), a series of solutions were added onto and removed from the RG surfaces sequentially from lowest concentrations to highest concentrations. For the selectivity test at 0.2 nM, analyte solutions including PFOS and other interferents were added onto and removed from the same RG surfaces one-by-one with thorough washing steps using blank tap water between different samples (the adsorption of all organic interferents is reversible at 0.2 nM

except the MB, which should be added at last in the sample sequence). For selectivity stress test, responses for PFOS at 1 ppt, 10 ppt and 100 ppt, organic interferents at 0.2 nM, 20 nM and 2,000 nM and inorganic ions at 100 ppb, 1 ppm and 10 ppm were recorded individually for different analytes to avoid potential irreversible adsorption at high concentrations.

**QCM**

The preparation of rGO-coated QCM sensor chips (Supplementary Fig.14) was modified from previous work by Melendrez et al.[41]. A gold QCM sensor (Biolin Scientific) was first sonicated in 2 wt.% SDS solutions and then in ethanol for 5 min. The chip was then treated with air plasma for 30 min. Afterward, 200 µL of 5 mg/mL GO ethanolic dispersion was spin-coated onto the QCM sensor surface at 2,000 rpm for 2.5 min (Laurell Technologies Corporation, model WS-650MZ-23NPP). Thermal annealing was conducted later at 180 °C for 6 h to sufficiently reduce GO to rGO while protecting the gold layer from destruction.

QCM measurements were performed using a QSense Analyzer (Biolin Scientific), recording 7 frequencies and dissipations. A stabilization process was conducted before any QCM measurements using the baseline solution at a flow rate of 300 µL/min until the drifting is less than 1 Hz/h. PBASE functionalization was monitored in-situ on rGO-coated QCM sensors using a 10 mg/mL solution in DMF for 2 h and then was washed thoroughly with DMF until the signal became flat. Afterward, the flowing solution was switched to DI water for a new round of baseline stabilization, then the $NH_2$-β-CD functionalization was recorded in-situ using a 0.2 mM solution in DI for ~ 17 h, and finally the surface was washed with copious DI flow until all the weakly-bounded molecules being removed. This two-step surface functionalization was recorded at a flow

26

rate of 25 µL/min at room temperature. The adsorption and desorption of PFOS, SDS, MB, and TCAA were performed at room temperature at a flow rate of 100 µL/min on β-CD-modified rGO-coated gold sensor surface. After flowing each sample solution, allow enough time for the adsorption to reach equilibrium state and then switch to the blank buffer solution for desorption until completion. The raw QCM data were fitted with various models built in the QSense Dfind software (all the frequencies and dissipations except the f1 and D1 were used in fitting) to obtain the surface mass density change curves, which were then converted to surface probe/analyte density curves by dividing the mass density by the molar mass of each target. The results from different model fitting were compared and the final model chosen for each measurement was determined by considering both the fitting quality and the real circumstances (material properties, adsorption nature, maximum allowable surface density, etc.). The maximum adsorbed analyte densities for different measurements were calculated and used for comparison.

## MD simulations

Simulations were conducted using the GROMACS 2021.6 simulation suite[45] employing the General Amber Force Field (GAFF2)[46] and the TIP3P water model[47]. To improve sampling of complex formation, we combined funnel metadynamics[48, 49] with well-tempered parallel bias metadynamics (PBMetaD)[50] implemented within PLUMED 2.8.1[51]. We used these calculations to recover an unbiased estimate of the potential of mean force, PMF(r, z), describing the relative free energy of various configurations of the probe-target system parameterized by the radial separation r and axial separation z of the molecular centers of mass within a coordinate frame centered on the β-CD probe (Fig. 4d, and Supplementary Fig. 20). These PMFs enable us to identify both the thermodynamically preferred binding locations for the PFOS analyte and SDS and TCAA

27

interferents with the β-CD probes and additionally make numerical predictions of the standard state equilibrium binding constants $K_b$ for quantitative comparison with previous experimental results. Full details of the simulations and calculation protocol are provided in the Supplementary Information (Supplementary Notes 1-3, Supplementary Figs. 20-23 and Supplementary Tables 4,5).

## Data availability

The data supporting the findings in this study are available within the paper and its Supplementary Information. Source data are provided with this paper.

## References

1.   Gluge, J. et al. An overview of the uses of per- and polyfluoroalkyl substances (PFAS). *Environ Sci Process Impacts* **22**, 2345-2373 (2020).
2.   Wang, Z., DeWitt, J.C., Higgins, C.P. & Cousins, I.T. A never-ending story of per- and polyfluoroalkyl substances (PFASs)? *Environ Sci Technol* **51**, 2508-2518 (2017).
3.   Evich, M.G. et al. Per- and polyfluoroalkyl substances in the environment. *Science* **375**, eabg9065 (2022).
4.   Lyu, X. et al. Per- and polyfluoroalkyl substances (PFAS) in subsurface environments: occurrence, fate, transport, and research prospect. *Reviews of Geophysics* **60** (2022).
5.   Jian, J.M. et al. A short review on human exposure to and tissue distribution of per- and polyfluoroalkyl substances (PFASs). *Sci Total Environ* **636**, 1058-1069 (2018).
6.   Fenton, S.E. et al. Per- and polyfluoroalkyl substance toxicity and human health review: current state of knowledge and strategies for informing future research. *Environ Toxicol Chem* **40**, 606-630 (2021).
7.   Sunderland, E.M. et al. A review of the pathways of human exposure to poly- and perfluoroalkyl substances (PFASs) and present understanding of health effects. *Journal of Exposure Science & Environmental Epidemiology* **29**, 131-147 (2019).
8.   Teymoorian, T., Munoz, G., Vo Duy, S., Liu, J. & Sauvé, S. Tracking PFAS in drinking water: A review of analytical methods and worldwide occurrence trends in tap water and bottled water. *ACS ES&T Water* **3**, 246-261 (2023).
9.   Sadia, M. et al. Occurrence, fate, and related health risks of PFAS in raw and produced drinking water. *Environ Sci Technol* **57**, 3062-3074 (2023).

10. Wang, Y., Darling, S.B. & Chen, J. Selectivity of per- and polyfluoroalkyl substance sensors and sorbents in water. *ACS Appl Mater Interfaces* **13**, 60789-60814 (2021).

11. Ryu, H., Li, B., De Guise, S., McCutcheon, J. & Lei, Y. Recent progress in the detection of emerging contaminants PFASs. *J Hazard Mater* **408**, 124437 (2021).

12. Rosenblum, L.W., S.C. in Method 533: Determination of per- and polyfluoroalkyl substances in drinking water by isotope dilution anion exchange solid phase extraction and liquid chromatography/tandem mass spectrometry (U.S. Environmental Protection Agency, 2019).

13. Shoemaker, J.A., Grimmett, P.E. & Boutin, B.K. in Method 537. Determination of selected perfluorinated alkyl acids in drinking water by solid phase extraction and liquid chromatography/tandem mass spectrometry (LC/MS/MS). (U.S. Environmental Protection Agency, 2009).

14. Ateia, M., Wei, H. & Andreescu, S. Sensors for emerging water contaminants: overcoming roadblocks to innovation. *Environmental Science & Technology* **58**, 2636-2651 (2024).

15. Zheng, Z. et al. Guanidinocalix[5]arene for sensitive fluorescence detection and magnetic removal of perfluorinated pollutants. *Nat Commun* **10**, 5762 (2019).

16. He, Y. et al. Porous adaptive luminescent metallacage for the detection and removal of perfluoroalkyl carboxylic acids. *Chem* **9**, 93-101 (2023).

17. Concellon, A., Castro-Esteban, J. & Swager, T.M. Ultratrace PFAS detection using amplifying fluorescent polymers. *J Am Chem Soc* **145**, 11420-11430 (2023).

18. Cheng, Y.H. et al. Metal-organic framework-based microfluidic impedance sensor platform for ultrasensitive detection of perfluorooctanesulfonate. *ACS Appl Mater Interfaces* **12**, 10503-10514 (2020).

19. Glasscott, M.W., Vannoy, K.J., Kazemi, R., Verber, M.D. & Dick, J.E. μ-MIP: molecularly imprinted polymer-modified microelectrodes for the ultrasensitive quantification of GenX (HFPO-DA) in river water. *Environmental Science & Technology Letters* **7**, 489-495 (2020).

20. Garada, M.B., Kabagambe, B., Kim, Y. & Amemiya, S. Ion-transfer voltammetry of perfluoroalkanesulfonates and perfluoroalkanecarboxylates: picomolar detection limit and high lipophilicity. *Anal Chem* **86**, 11230-11237 (2014).

21. Dasetty, S. et al. Data-driven discovery of linear molecular probes with optimal selective affinity for PFAS in water. *Journal of Chemical & Engineering Data* **68**, 3148-3161 (2023).

22. Chen, J., Pu, H., Hersam, M.C. & Westerhoff, P. Molecular engineering of 2D nanomaterial field-effect transistor sensors: fundamentals and translation across the innovation spectrum. *Advanced Materials* **34**, 2106975 (2022).

23. Li, Y. et al. Fully integrated graphene electronic biosensor for label-free detection of lead (II) ion based on G-quadruplex structure-switching. *Biosens Bioelectron* **89**, 758-763 (2017).

24. Maity, A. et al. Scalable graphene sensor array for real-time toxins monitoring in flowing water. *Nature Communications* **14**, 4184 (2023).

25. Chen, X. et al. Real-time and selective detection of nitrates in water using graphene-based field-effect transistor sensors. *Environmental Science: Nano* **5**, 1990-1999 (2018).

26. Bhat, K.S., Ahmad, R., Mahmoudi, T. & Hahn, Y.-B. High performance chemical sensor with field-effect transistors array for selective detection of multiple ions. *Chemical Engineering Journal* **417**, 128064 (2021).

27.    Yeor-Davidi, E., Zverzhinetsky, M., Krivitsky, V. & Patolsky, F. Real-time monitoring of bacterial biofilms metabolic activity by a redox-reactive nanosensors array. *J Nanobiotechnology* **18**, 81 (2020).

28.    Thakur, B. et al. Rapid detection of single E. coli bacteria using a graphene-based field-effect transistor device. *Biosensors and Bioelectronics* **110**, 16-22 (2018).

29.    Jang, H.J. et al. Remote floating-gate field-rffect transistor with 2-dimensional reduced graphene oxide sensing layer for reliable detection of SARS-CoV-2 spike proteins. *ACS Appl Mater Interfaces* **14**, 24187-24196 (2022).

30.    Jang, H.J. et al. Analytical platform To characterize dopant solution concentrations, charge carrier densities in films and interfaces, and physical diffusion in polymers utilizing remote field-effect transistors. *J Am Chem Soc* **141**, 4861-4869 (2019).

31.    Jang, H.J. et al. Rapid, sensitive, label-free electrical detection of SARS-CoV-2 in nasal swab samples. *ACS Appl Mater Interfaces* **15**, 15195-15202 (2023).

32.    Xiao, L. et al. beta-Cyclodextrin polymer network sequesters perfluorooctanoic acid at environmentally relevant concentrations. *J Am Chem Soc* **139**, 7689-7692 (2017).

33.    Weiss-Errico, M.J., Ghiviriga, I. & O'Shea, K.E. (19)F NMR characterization of the encapsulation of emerging perfluoroethercarboxylic acids by cyclodextrins. *J Phys Chem B* **121**, 8359-8366 (2017).

34.    Wang, W. et al. Rapid removal of perfluoroalkanesulfonates from water by beta-cyclodextrin covalent organic frameworks. *ACS Appl Mater Interfaces* **13**, 48700-48708 (2021).

35.    Lowe, B.M., Skylaris, C.K., Green, N.G., Shibuta, Y. & Sakata, T. Molecular dynamics simulation of potentiometric sensor response: the effect of biomolecules, surface morphology and surface charge. *Nanoscale* **10**, 8650-8666 (2018).

36.    Dinelli, E. et al. Major and trace elements in tap water from Italy. *Journal of Geochemical Exploration* **112**, 54-75 (2012).

37.    Kumarasamy, E., Manning, I.M., Collins, L.B., Coronell, O. & Leibfarth, F.A. Ionic fluorogels for remediation of per- and polyfluorinated alkyl substances from water. *ACS Central Science* **6**, 487-492 (2020).

38.    Koda, Y., Terashima, T. & Sawamoto, M. Fluorous microgel star polymers: selective recognition and separation of polyfluorinated surfactants and compounds in water. *J Am Chem Soc* **136**, 15742-15748 (2014).

39.    Zhao, F. et al. EDTA-cross-linked β-cyclodextrin: an environmentally friendly bifunctional adsorbent for simultaneous adsorption of metals and cationic dyes. *Environmental Science & Technology* **49**, 10570-10580 (2015).

40.    Lee, J. et al. Ultra-high capacity, multifunctional nanoscale sorbents for PFOA and PFOS treatment. *npj Clean Water* **6** (2023).

41.    Melendrez, D. et al. Adsorption and binding dynamics of graphene-supported phospholipid membranes using the QCM-D technique. *Nanoscale* **10**, 2555-2567 (2018).

42.    Du, Z. et al. Adsorption behavior and mechanism of perfluorinated compounds on various adsorbents--a review. *J Hazard Mater* **274**, 443-454 (2014).

43.    Weiss-Errico, M.J. & O'Shea, K.E. Detailed NMR investigation of cyclodextrin-perfluorinated surfactant interactions in aqueous media. *J Hazard Mater* **329**, 57-65 (2017).

44.    Humphrey, W., Dalke, A. & Schulten, K. VMD: Visual molecular dynamics. *Journal of Molecular Graphics* **14**, 33-38 (1996).

45. Abraham, M.J. et al. GROMACS: High performance molecular simulations through multi-level parallelism from laptops to supercomputers. *SoftwareX* **1-2**, 19-25 (2015).

46. He, X., Man, V.H., Yang, W., Lee, T.-S. & Wang, J. A fast and high-quality charge model for the next generation general AMBER force field. *The Journal of Chemical Physics* **153**, 114502 (2020).

47. Jorgensen, W.L., Chandrasekhar, J., Madura, J.D., Impey, R.W. & Klein, M.L. Comparison of simple potential functions for simulating liquid water. *The Journal of Chemical Physics* **79**, 926-935 (1983).

48. Limongelli, V., Bonomi, M. & Parrinello, M. Funnel metadynamics as accurate binding free-energy method. *Proceedings of the National Academy of Sciences* **110**, 6358-6363 (2013).

49. Rizzi, V., Bonati, L., Ansari, N. & Parrinello, M. The role of water in host-guest interaction. *Nature Communications* **12**, 93 (2021).

50. Pfaendtner, J. & Bonomi, M. Efficient sampling of high-dimensional free-energy landscapes with parallel bias metadynamics. *Journal of Chemical Theory and Computation* **11**, 5062-5067 (2015).

51. Bonomi, M. et al. PLUMED: A portable plugin for free-energy calculations with molecular dynamics. *Computer Physics Communications* **180**, 1961-1972 (2009).

# Acknowledgements

## Author contributions

Y.W., S.B.D. and J.C designed the project, analyzed data, and prepared the manuscript. Y.W. performed the sensor fabrication, majority of the surface characterization (WCA, SEM, AFM and Raman), sample preparation, sensor testing, QCM experiments, and analyzed the data. H.J. designed the RGFET sensing platform in this work, analyzed the data and revised the manuscript. M.T., S.D. and A.L.F. conducted the MD simulations and wrote the analysis for simulation results. Y.L. performed the ICP and TOC experiments and wrote Python codes for sensor data processing. A.T. performed the LC-MS/MS measurement and M.A. analyzed the data. V.R. and J.W.E. conducted the XPS measurement and analyzed the data. E.O. assisted in sensor fabrication, sample preparation and sensor testing. W. Z. assisted in sensor fabrication and data analysis. H.P. assisted in data analysis and interpretation and revised the manuscript. S.S.L. assisted in AFM measurement

and analyzed the data. S.B.D. and J.C. supervised and managed the project. All authors reviewed and edited the manuscript.

## Disclaimer

This document has been subjected to the U.S. Environmental Protection Agency's review and has been approved for publication. The views expressed in this article are those of the authors and do not necessarily represent the views or policies of the Agency. Any mention of trade names, products or services does not imply an endorsement by the Agency. The Agency does not endorse any commercial products, services, or enterprises.

## Competing interests

A.L.F. is a co-founder and consultant of Evozyne, Inc. and a co-author of US Patent Applications 16/887,710 and 17/642,582, US Provisional Patent Applications 62/853,919, 62/900,420, 63/314,898, 63/479,378, and 63/521,617, and International Patent Applications PCT/US2020/035206 and PCT/US2020/050466. J.C. is a founder and consultant of NanoAffix Science LLC. Neither Evozyne nor NanoAffix funded the research reported here.

## Additional Information

Supplementary information: The online version contains supplementary material available at xxx.